Autotaxin-LPA signaling contributes to obesity-induced insulin resistance in muscle and impairs mitochondrial metabolism[S]

Kenneth D'Souza,* Carine Nzirorera,* Andrew M. Cowie,* Geena P. Varghese,* Purvi Trivedi,* Thomas O. Eichmann,† Dipsikha Biswas,* Mohamed Touaibia,§ Andrew J. Morris, Vassilis Aidinis,†† Daniel A. Kane,§§ Thomas Pulinilkunnil,* and Petra C. Kienesberger[1],***

Dalhousie Medicine New Brunswick,* Department of Biochemistry and Molecular Biology, Dalhousie University, Saint John, New Brunswick E2L 4L5, Canada; Institute of Molecular Biosciences,† University of Graz and Center for Explorative Lipidomics, BioTechMed-Graz, 8010 Graz, Austria; Department of Chemistry and Biochemistry,§ Université de Moncton, Moncton, New Brunswick E1A 3E9, Canada; Division of Cardiovascular Medicine,** University of Kentucky, Lexington, KY 40536 and Lexington Veterans Affairs Medical Center, Lexington, KY 40511; Division of Immunology,†† Biomedical Sciences Research Center "Alexander Fleming", 16672 Athens, Greece; and Department of Human Kinetics,§§ St. Francis Xavier University, Antigonish, Nova Scotia B2G 2W5, Canada

ORCID IDs: 0000-0002-2734-188X (K.D.); 0000-0002-8521-2795 (T.O.E.); 0000-0001-9531-7729 (V.A.); 0000-0003-1228-893X (T.P.); 0000-0001-9643-8338 (P.C.K.)

Abstract Autotaxin (ATX) is an adipokine that generates the bioactive lipid, lysophosphatidic acid (LPA). ATX-LPA signaling has been implicated in diet-induced obesity and systemic insulin resistance. However, it remains unclear whether the ATX-LPA pathway influences insulin function and energy metabolism in target tissues, particularly skeletal muscle, the major site of insulin-stimulated glucose disposal. The objective of this study was to test whether the ATX-LPA pathway impacts tissue insulin signaling and mitochondrial metabolism in skeletal muscle during obesity. Male mice with heterozygous ATX deficiency (ATX$^{+/-}$) were protected from obesity, systemic insulin resistance, and cardiomyocyte dysfunction following high-fat high-sucrose (HFHS) feeding. HFHS-fed ATX$^{+/-}$ mice also had improved insulin-stimulated AKT phosphorylation in white adipose tissue, liver, heart, and skeletal muscle. Preserved insulin-stimulated glucose transport in muscle from HFHS-fed ATX$^{+/-}$ mice was associated with improved mitochondrial pyruvate oxidation in the absence of changes in fat oxidation and ectopic lipid accumulation. Similarly, incubation with LPA decreased insulin-stimulated AKT phosphorylation and mitochondrial energy metabolism in C2C12 myotubes at baseline and following palmitate-induced insulin resistance. Taken together, our results suggest that the ATX-LPA pathway contributes to obesity-induced insulin resistance in metabolically relevant tissues. Our data also suggest that LPA directly impairs skeletal muscle insulin signaling and mitochondrial function.—D'Souza, K., C. Nzirorera, A. M. Cowie, G. P. Varghese, P. Trivedi, T. O. Eichmann, D. Biswas, M. Touaibia, A. J. Morris, V. Aidinis, D. A. Kane, T. Pulinilkunnil, and P. C. Kienesberger. **Autotaxin-LPA signaling contributes to obesity-induced insulin resistance in muscle and impairs mitochondrial metabolism.** ***J. Lipid Res.*** **2018.** 59: **1805–1817.**

Supplementary key words diet effects/lipid metabolism • glucose • pyruvate • skeletal muscle • respiration

Autotaxin (ATX) is a lysophospholipase D that is also known as ecto-nucleotide pyrophosphatase/phosphodiesterase family member 2 (ENPP2) (1), and generates the majority of extracellular lysophosphatidic acid (LPA) by hydrolyzing the lysophosphatidylcholine (LPC) contained

This work was supported by Natural Sciences and Engineering Research Council of Canada Discovery Grant RGPIN-2014-04454, Canadian Institutes of Health Research Project Grant 156308, and grants from the Banting Research Foundation, the New Brunswick Health Research Foundation, the New Brunswick Innovation Foundation, and the Heart and Stroke Foundation of Canada to P.C.K. Additional support was provided by the Natural Sciences and Engineering Research Council of Canada, the Canadian Diabetes Association, the New Brunswick Health Research Foundation, the New Brunswick Innovation Foundation, and the Canada Foundation for Innovation to T.P. The authors declare that no conflict of interest exists.

Manuscript received 27 November 2017 and in revised form 26 June 2018.

Published, JLR Papers in Press, August 2, 2018
DOI https://doi.org/10.1194/jlr.M082008

Abbreviations: ATX, autotaxin; BAT, brown adipose tissue; DG, diacylglycerol; FAF, fatty acid-free; FCCP, carbonyl cyanide-4-(trifluoromethoxy)phenylhydrazone; fwd, forward; GTT, glucose tolerance test; HFHS, high-fat high-sucrose; ITT, insulin tolerance test; JNK, c-Jun N-terminal kinase; KHB, Krebs-Henseleit bicarbonate buffer; LPC, lysophosphatidylcholine; LPA, lysophosphatidic acid; MIR05, mitochondrial respiration medium; PGAT, perigonadal adipose tissue; rev, reverse; TG, triacylglycerol.

[1] To whom correspondence should be addressed.
e-mail: pkienesb@Dal.Ca

[S] The online version of this article (available at http://www.jlr.org) contains a supplement.

in lipoproteins and activated platelets (1–3). Despite its ubiquitous expression, a substantial proportion of circulating ATX emanates from the adipose tissue. Indeed, adipose-specific ATX knockout mice exhibit ~50% reduced plasma LPA (4, 5). ATX-LPA signaling through G protein-coupled receptors (LPA1–6) influences many biological processes, including brain development, embryo implantation, vasculogenesis, and hair follicle formation (6). Signaling effectors downstream of LPA receptors include PI3Kinase-AKT-Ras-related C3 botulinum toxin substrate 1 activation, modulation of adenylate cyclase, stimulation of the mitogen-activated protein kinase pathway, Rho and Rho kinase activation, and stimulation of the phospholipase C-protein kinase C pathway (7).

The ATX-LPA signaling axis plays an important role in many disease states, such as cancer, cardiovascular disease, neuropathic pain, pulmonary fibrosis, and arthritis (2, 8–12). Notably, the ATX-LPA axis has been explored as a therapeutic target in diseases associated with chronic inflammation (13, 14). At least three compounds targeting the ATX-LPA pathway have passed phase I and II clinical trials for the treatment of idiopathic pulmonary fibrosis and systemic sclerosis (13, 15), demonstrating that modulators of ATX-LPA receptor signaling have promising therapeutic potential. A recent study showed that genetic deletion or long-term pharmacologic inhibition of ATX in adult mice is well-tolerated, alleviating concerns that targeting the ATX-LPA pathway could elicit toxicity (16).

The ATX-LPA pathway has also been implicated in obesity and metabolic disease, specifically insulin resistance and impaired glucose homeostasis (4, 5, 17–22). In humans, serum ATX correlates with measures of obesity, impaired glucose homeostasis, and insulin resistance (19, 20). In addition, serum ATX is independently associated with hepatic steatosis, a metabolic complication of obesity and diabetes, in severely obese women (19). Studies in mice showed that ATX-LPA signaling influences adiposity, although it remains incompletely understood whether the ATX-LPA pathway promotes or protects from diet-induced obesity and adipocyte hypertrophy (4, 5, 23). Dusaulcy et al. (4) showed that high-fat-fed adipose-specific ATX knockout mice have increased fat mass and adipocyte size. On the other hand, Nishimura et al. (5) demonstrated that adipose-specific and global heterozygous ATX knockout ($ATX^{+/-}$) mice are protected from high-fat diet-induced obesity (5). Brown adipose tissue (BAT) was functionally more active, resulting in increased energy expenditure in ATX-deficient mice (5). Moreover, ATX overexpression in mice led to augmented obesity following high-fat feeding (5, 23). Regardless of the effect of ATX-LPA on adiposity, studies using global heterozygous or fat-specific ATX knockout mice suggest that the ATX-LPA pathway contributes to high-fat diet-induced systemic insulin resistance and impaired glucose homeostasis (4, 5). Consistent with these studies, acute LPA injection resulted in impaired glucose tolerance in chow- and high-fat diet-fed mice through inhibition of glucose-induced insulin secretion, an effect that was blunted by Ki16425, a preferential LPA1/3 antagonist (24). Prolonged administration of Ki16425 for 3 weeks enhanced glucose tolerance and insulin sensitivity in high-fat diet-fed mice in the absence of changes in adiposity, which was mainly ascribed to increased islet cell number, glycogen storage in the liver, and muscle glucose oxidation (24).

Despite growing evidence suggesting that the ATX-LPA pathway impacts glucose homeostasis and global insulin sensitivity in mice and humans, it remains unclear whether ATX-LPA signaling influences insulin sensitivity through direct or indirect effects of LPA on insulin target tissues. In particular, it is incompletely understood whether the ATX-LPA pathway modulates insulin function and energy metabolism in skeletal muscle, which accounts for the majority of insulin-mediated glucose disposal (25). Therefore, we examined tissue insulin signaling in mice with global heterozygous ATX deficiency subjected to diet-induced obesity and tested to determine whether the ATX-LPA pathway influences glucose and lipid metabolism in skeletal muscle.

Our study shows that: *1*) partial ATX deficiency protects from impaired insulin signaling in white adipose tissue, liver, heart, and skeletal muscle following high-fat high-sucrose (HFHS) feeding, as is reflected in reduced weight gain, improved glucose and insulin tolerance, and blunted cardiomyocyte dysfunction in male HFHS-fed $ATX^{+/-}$ mice; *2*) HFHS-fed $ATX^{+/-}$ mice are resistant to impaired insulin-stimulated glucose transport in skeletal muscle and have improved mitochondrial pyruvate oxidation; and *3*) in C2C12 myotubes, incubation with LPA reduces insulin-stimulated AKT phosphorylation at baseline and exacerbates palmitate-induced insulin resistance, coincident with impaired mitochondrial respiration. Taken together, these data suggest that the ATX-LPA pathway negatively regulates muscle insulin signaling and mitochondrial function.

MATERIALS AND METHODS

Chemicals and reagents

Unless otherwise stated, chemicals and reagents were obtained from Sigma.

Animals

The generation of $ATX^{+/-}$ mice (C57Bl/6-Enpp2<tm1.1Vart>/FLMG) and genotyping instructions have been previously reported (26). Briefly, loxP-flanked neomycin selection cassettes were inserted upstream of exon 1 and downstream of exon 2 (26). Transgenic expression of Cre recombinase in mice bearing this allele resulted in excision of both exons, thus abolishing protein expression. Mice were housed on a 12 h light:12 h dark cycle with ad libitum access to chow diet (LD5001 from LabDiet with 13.5 kcal% from fat) or HFHS diet (12451 from Research Diets with 45 kcal% from fat and 17 kcal% from sucrose) and water. Male and female mice (7–9 weeks old) were randomly assigned to chow or HFHS cohorts and fed for 20 weeks. For food intake studies, mice were individually housed and food consumption was monitored daily over a 5 day period 2 weeks post diet start. Mice were subjected to an insulin tolerance test (ITT) or glucose tolerance test (GTT) at 15 and 17 weeks post diet start, respectively. Peripheral fat accumulation in isofluorane-anesthetized mice was determined by X-ray imaging using a Bruker In-Vivo Xtreme imager 18 weeks post diet start. Planar X-ray images were analyzed using ImageJ software (National Institutes of Health) and area of peripheral fat was expressed as percent of total body area. Mice were euthanized by decapitation following a 3 h food withdrawal and tissues were collected. Perigonadal adipose tissue (PGAT) and BAT were weighed prior to being flash-frozen. EDTA-plasma was collected and spun at 15,600 *g* for 10 min at 4°C. For serum collection, blood was spun at 2,000 *g* for 15 min at 4°C. Plasma and serum were frozen and stored at −80°C until further use. All protocols involving mice were approved by the Dalhousie University Institutional Animal Care and Use Committee.

ITTs and GTTs

ITTs and GTTs were performed as previously described (27). For ITTs, awake mice were injected intraperitoneally with 1 U human insulin (HumulinR; Eli Lilly) per kilogram body weight following a 3 h food withdrawal. For GTTs, awake 16 h-fasted mice were injected intraperitoneally with 20% (w/v) D-glucose at 2 g/kg body weight. Blood glucose was measured using an Aviva Nano glucometer (Accu-Chek).

Insulin signaling studies

For insulin signaling studies performed in vivo, mice were injected intraperitoneally with 10 U of insulin per kilogram body weight or an equal volume of saline. After 10 min, mice were euthanized and tissues were collected. For ex vivo insulin signaling studies in muscle, isolated soleus muscles were preincubated for 30 min in pregassed (95% O_2, 5% CO_2) Krebs-Henseleit bicarbonate buffer (KHB) (pH 7.4) (118.5 mM NaCl, 4.7 mM KCl, 1.2 mM KH_2PO_4, 25 mM $NaCHO_3$, 2.5 mM $CaCl_2$, 1.2 mM $MgSO_4$, and 5 mM HEPES) at 37°C. Following subsequent incubation in buffer with or without 33 nM insulin for 10 min, muscles were removed; connective tissue, fat, and tendons were excised; and tissues were blotted dry and snap-frozen in liquid nitrogen.

Muscle glucose transport assay

Glucose transport in soleus muscle was determined ex vivo as previously described (27), with slight modifications. Soleus muscles from mice were rapidly dissected, preincubated for 1 h in KHB containing 10 mM D-glucose at 37°C, and rinsed by incubation in KHB supplemented with 10 mM D-mannitol for 10 min. Glucose transport was assessed by incubation in KHB with 1 mM 2-deoxyglucose, 9 mM mannitol, 1.5 μCi/ml 2-deoxy-D-[1,2-^{3}H] glucose (Perkin Elmer), and 0.3 μCi/ml D-[1-^{14}C]mannitol (Perkin Elmer) for 20 min at 37°C. All buffers were pregassed with 95% O_2, 5% CO_2 and were supplemented with saline or 33 nM insulin. Basal glucose transport and insulin-stimulated glucose transport were determined in contralateral muscles. Following the final incubation, muscles were cleaned by excising connective tissue, fat, and tendons, and tissues were blotted dry and snap-frozen in liquid nitrogen. Muscles were weighed and digested for 30 min in 300 μl of 1 N NaOH at 65°C and centrifuged at 13,000 *g* for 10 min. Radioactivity in the supernatant was determined by liquid scintillation counting and glucose transport into tissues was calculated.

Gene expression analysis

RNA isolation, reverse transcription, and real-time quantitative PCR were performed as previously described (22, 28) using the following primer sequences: *Glut1*-forward (fwd) 5′-GGTGTGCAGCAGCCTGTGTACG-3′, *Glut1*-reverse (rev) 5′-TAGGACATCCAAGGCAGCCGTTC-3′, *Glut4*-fwd 5′-ACCGGCAGCCTCTGATCATCG-3′, *Glut4*-rev 5′-GAGTGTCCGTCGTCCAGCTCGTT-3′, *Rpl27*-fwd 5′-ACGGTGGAGCCTTATGTGAC-3′, *Rpl27*-rev 5′-TCCGTCAGAGGGACTGTCTT-3′, *Rpl41*-fwd 5′-GCCATGAGAGCGAAGTGG-3′, and *Rpl41*-rev 5′-CTCCTGCAGGCGTCGTAG-3′.

Plasma and serum analysis

Serum insulin was determined using an ELISA kit assay (Crystal Chem). NEFA (WAKO Chemicals) and triacylglycerol (TG) (Thermo Fisher Scientific) analyses were performed using colorimetric kit assays, as per the manufacturer's instructions. Plasma LPA levels were determined by HPLC/ESI/MS/MS analysis as previously described (29).

Cell culture

Insulin resistance was induced in C2C12 cells as previously described (28). Briefly, cells were incubated in medium containing 2% (w/v) fatty acid-free (FAF)-BSA and 0.8 mM sodium palmitate for 16–18 h. Myotubes were cultured with 2% FAF-BSA in the absence of palmitate to mimic an insulin-sensitive state. To examine insulin signaling, cells were incubated with 100 nM insulin or PBS for 15 min. Cells were washed once and harvested in ice-cold PBS, followed by centrifugation at 20,000 *g* for 10 min at 4°C. Cell pellets were flash-frozen in liquid nitrogen and stored at −80°C until further use. For experiments involving LPA, 1-oleoyl-2-hydroxy-*sn*-glycero-3-phosphate (18:1 LPA; Avanti) was dissolved in PBS with 0.1% FAF-BSA, gently shaken, and mixed with DMEM-1X supplemented with 5 mM glucose prior to its addition to C2C12 myotubes. Cells were cultured in the absence of serum during LPA treatment to avoid potential additional sources of LPA, LPC, and ATX.

Assessment of ATX activity

ATX activity in plasma and serum was quantified as previously described (22, 30). Briefly, 2 μl of plasma or serum were added to 18 μl of buffer A containing 100 mM Tris-HCl (pH 9.0), 500 mM NaCl, 5 mM $MgCl_2$, and 0.05% v/v Triton X-100. For samples examined in the presence of the ATX inhibitor, PF-8380 (31), 5 μl of buffer A containing 10% DMSO or 5 mM of PF-8380 were added. Samples were preincubated at 37°C for 30 min and 25 μl of 6 mM 1-myristoyl-2-hydroxy-*sn*-glycero-3-phosphocholine (14:0 LPC; Avanti) were added. The reaction mixture was incubated at 37°C for 6 h to allow for ATX-mediated choline release. Subsequently, 20 μl of sample were incubated with 90 μl of buffer C {9.65 ml of buffer B [100 mM Tris-HCl (pH 8.5) and 5 mM $CaCl_2$], 110 μl of 30 mM *N*-ethyl-*N*-(2-hydroxy-3-sulfopropyl)-3-methylaniline (TOOS; Cedarlane), 110 μl of 50 mM 4-aminotipyrine, 6.6 μl of 1,000 U/ml horseradish peroxidase, and 110 μl of 300 U/ml choline oxidase} at 37°C for 20 min and choline oxidation was recorded at 550 nm for 30 min.

Immunoblotting analysis

Tissues and cells were homogenized in lysis buffer [20 mM Tris-HCl (pH 7.5), 5 mM EDTA, 10 mM $Na_4P_2O_7$, 100 mM NaF, and 1% NP-40] containing 2 mM sodium orthovanadate, 2 mM protease inhibitor cocktail (P8340; Sigma), and 100 μg/ml phosphatase inhibitor cocktail (524628; Calbiochem) using a tissue homogenizer (Omni TH; Omni International) or by sonication, respectively. Protein concentrations in tissue and cell lysates or plasma were quantified colorimetrically using a BCA protein assay kit (Thermo Scientific) and BSA as standard. Lysates or plasma were subjected to SDS-PAGE and proteins were transferred onto a nitrocellulose membrane. Proteins were visualized using a reversible protein stain (Memcode; Pierce, Thermo Fisher Scientific) and membranes were incubated with the following primary antibodies: anti-pAKT S^{473} (9271; Cell Signaling), anti-AKT (05-591; Millipore), anti-pp70S6K T^{389} (9234; Cell Signaling), anti-p70S6K

(2708; Cell Signaling), anti-pERK T^{202}/Y^{204} (9101; Cell Signaling), anti-ERK (9102; Cell Signaling), anti-pJNK T^{183}/Y^{185} (4688; Cell Signaling), and anti-c-Jun N-terminal kinase (JNK) (9252; Cell Signaling). Immunoblots were developed using the Western Lightning Plus-ECL enhanced chemiluminescence substrate (Perkin Elmer). Densitometric analysis was performed using Image Lab software (Bio-Rad).

Mitochondrial analysis

Respiratory oxygen flux in permeabilized soleus muscle fibers and C2C12 myotubes was measured in high-resolution using the Oxygraph-2k (OROBOROS Instruments). Permeabilized fibers were prepared as described (32). Briefly, soleus muscles were incubated in ice-cold biopsy preservation solution [10 mM Ca-EGTA buffer, 0.1 μM free Ca, 20 mM imidazole, 20 mM taurine, 50 mM K-MES, 0.5 mM DTT, 6.56 mM $MgCl_2$, 5.77 mM ATP, and 15 mM phosphocreatine (pH 7.1)]. Excess connective tissue, fat, and tendons were removed and fiber bundles were mechanically separated using forceps. Fiber bundles were permeabilized in 2 ml of biopsy preservation solution containing 50 μg/ml saponin and gently agitated on ice for 30 min. Thereafter, fiber bundles were washed in mitochondrial respiration medium (MiR05) buffer (0.5 mM EGTA, 3 mM $MgCl_2$-$6H_2O$, 60 mM lactobionic acid, 20 mM taurine, 10 mM KH_2PO_4, 20 mM HEPES, 110 mM sucrose, and 1 g/l FAF-BSA); fiber wet weights were obtained; and samples were placed in the Oxygraph chambers. Samples were assessed in 2 ml of hyper-oxygenated MiR05 buffer at 37°C and reoxygenated as necessary throughout the protocol. Instrumental background O_2 consumption was corrected using equations determined under the same parameters used for experimental data collection. C2C12 myotubes (200,000 cells/ml) were incubated with saline or 10 μM LPA for 16 h prior to cell permeabilization with 3 μg/ml digitonin and mitochondrial respiration analysis. Thereafter, cells were collected and stored at −80°C until further analysis. The respirometric protocol for muscle fibers and C2C12 myotubes involved the sequential addition of substrates, inhibitors, and/or titration of substrates, as indicated. Mitochondrial respiration was normalized to protein content, as determined by a BCA assay.

Citrate synthase activity assay

Citrate synthase activity was determined as previously described, with minor modifications (33). Permeabilized skeletal muscle fibers or C2C12 cell pellets were homogenized in buffer containing 20 mM HEPES, 10 mM EDTA, and 10 μl/ml protease inhibitor (pH 7.4), and incubated on ice for 30 min. Samples were spun at 600 *g* for 20 min at 4°C. An aliquot of the supernatant was used to determine protein concentration using a BCA assay. Homogenates were frozen for 1 h at −80°C to liberate citrate synthase from the mitochondrial matrix. The reaction was initiated by the addition of 227.5 μl of reaction buffer containing 20 mM HEPES, 2 mM EGTA, 220 mM sucrose, 40 mM KCl, 0.1 mM DTNB, and 0.3 mM acetyl-CoA (pH 7.4) at 25°C. After 5 min, a baseline reading was obtained at 412 nm. The reaction was started by the addition of 0.5 mM oxaloacetate and monitored at 412 nm for 10 min.

Tissue lipid analysis

For targeted lipidomic analysis in muscle, total lipids of weighed muscle tissue explants (50–100 mg) were extracted twice according to Folch, Lees, and Sloane Stanley (34) using 4 ml chloroform/methanol (2/1, v/v) containing 500 pmol of butylated hydroxytoluene, 1% acetic acid, and 100 pmol of internal standards (d18:1/17:0 ceramide, 14:0-14:0 diacylglycerol (DG), 15:0-15:0-15:0 TG; Avanti Polar Lipids) per sample. Extraction was performed under constant shaking for 90 min at room temperature. After addition of 800 μl of dH_2O and further incubation for 30 min at room temperature, samples were spun at 1,000 *g* for 15 min at room temperature to establish phase separation. The lower organic phase was collected, 2.5 ml of chloroform were added to the remaining aqueous phase, and the second extraction was performed as described above (30 min at room temperature with subsequent centrifugation). Combined organic phases of the double-extraction were dried under a stream of nitrogen and lipids were resolved in 150 μl of 2-propanol/methanol/water (6/3/1, v/v/v) for UPLC-MS analysis. For protein determination, the interphase was dried and lysed using 1.5 ml NaOH/SDS (0.3 N/0.1%).

Chromatographic separation was modified after Knittelfelder et al. (35) using an AQUITY-UPLC system (Waters Corporation) equipped with a Kinetex EVO-C18 column (2.1 × 50 mm, 1.7 μm; Phenomenex), starting a 15 min linear gradient with 100% solvent A (methanol/water, 1/1, v/v; 10 mM ammonium acetate, 0,1% formic acid, and 8 μM phosphoric acid).

An EVOQ Elite™ triple quadrupole mass spectrometer (Bruker) equipped with an ESI source was used for detection. Lipid species were analyzed by selected reaction monitoring (DG: $[MNH4]^+$ to $[RCOO+58]^+$ of the respective esterified fatty acid, 15 eV, 50 ms; TG: $[MNH4]^+$ to $[DG\text{-}H_2O]^+$ of the respective DG, 23eV, 30 ms; Ceramide: $[MH]^+$ to *m/z* 264.3, 22 eV, 60 ms; the resolution of Q1/Q3 were set to 0.7). Data were acquired with MS Workstation (Bruker). Data were normalized for recovery, extraction, and ionization efficacy by calculating analyte/internal standard ratios (AU) and expressed as AU per milligram of tissue protein.

Analysis of TG accumulation in the liver (20 mg) was performed using a colorimetric assay (Infinity Triglycerides reagent; Thermo Fisher Scientific) as previously described (36).

Adult ventricular cardiomyocyte culture and sarcomere shortening analysis

Cardiomyocytes were isolated from mice as previously described (37). Cells were seeded on laminin-coated coverslips (4,000 cells/cm^2) in plating medium. Following a 2 h incubation, cardiomyocytes were transferred to EBSS medium (Thermo Fisher Scientific) containing 1.25 mM Ca and electrically stimulated at 1 Hz. Sarcomere dimensions during contractions were assessed using a PTI RatioMaster monochromator-based wide-field microscope system (Horiba) in single cardiomyocytes. Sarcomere length, fractional shortening {[(sarcomere length at peak of relaxation – sarcomere length at peak of contraction)/sarcomere length at peak of relaxation] × 100}, sarcomere shortening rate, and sarcomere relengthening rate were determined.

Statistical analysis

Results are expressed as mean ± SEM. Comparisons between two groups were performed using an unpaired two-tailed Student's *t*-test. Comparisons between multiple groups were performed using a paired or unpaired one- or two-way ANOVA followed by a Tukey or Sidak post hoc test, as appropriate. All statistical analysis was performed using Prism (GraphPad Software). *P* values of less than 0.05 were considered statistically significant.

RESULTS

Male mice with heterozygous ATX deficiency have reduced obesity and improved glucose homeostasis on an obesogenic "Western" diet

Although prior studies have suggested that ATX haploinsufficiency or adipocyte-specific ATX deficiency improves systemic glucose homeostasis in mice fed a high-fat diet, the effect of ATX deficiency on obesity and tissue insulin signaling remains unclear (4, 5). To clarify the role of ATX in diet-induced obesity, glucose metabolism, and insulin signaling, we fed male WT and $ATX^{+/-}$ mice chow or HFHS diet for 20 weeks. In agreement with previous studies (5, 26), plasma LPA levels, ATX activity, and ATX protein content were markedly reduced in $ATX^{+/-}$ mice compared with WT mice (supplemental Fig. S1A–E). Body weights were similar between WT and $ATX^{+/-}$ mice immediately prior to HFHS feeding (WT, 22.45 ± 0.26 g; $ATX^{+/-}$, 22.30 ± 0.56 g; n = 15–18). However, HFHS-fed $ATX^{+/-}$ mice showed significantly reduced body weight gain compared with HFHS-fed WT mice, while food intake was unchanged between genotypes (**Fig. 1A**, B). In agreement with lower body weight gain, HFHS-fed $ATX^{+/-}$ mice showed reduced peripheral fat accumulation and PGAT and BAT weights (Fig. 1C–E). Furthermore, HFHS-fed $ATX^{+/-}$ mice had improved glucose tolerance and insulin sensitivity, as assessed by a GTT and an ITT, respectively (Fig. 1F, G). $ATX^{+/-}$ mice were also protected from HFHS diet-induced hyperglycemia (Fig. 1H), hyperinsulinemia (Fig. 1I), and hypertriglyceridemia (Fig. 1J), while serum NEFA levels were similar between groups (Fig. 1K). Taken together, these data suggest that partial ATX deficiency protects from diet-induced obesity and impaired glucose and lipid homeostasis in male mice.

HFHS-induced body weight gain was much less pronounced in female mice and was unchanged between genotypes (supplemental Fig. S2A). Modest body weight gain in female HFHS-fed WT mice was associated with unchanged serum ATX activity (supplemental Fig. S2B) and insulin-stimulated AKT phosphorylation in muscle when compared with chow-fed mice (supplemental Fig. S2C, D). Therefore, subsequent studies were performed in male mice.

HFHS-fed $ATX^{+/-}$ mice have improved insulin signaling in liver, white adipose tissue, heart, and skeletal muscle

To examine whether enhanced tissue insulin function underlies the improvement in glucose homeostasis in HFHS-fed $ATX^{+/-}$ mice, we performed in vivo insulin signaling analysis in metabolically relevant tissues. HFHS-fed WT mice developed insulin resistance in the liver and PGAT, as was evidenced by a 2- to 3-fold decrease in insulin-stimulated phosphorylation of AKT at S^{473} (**Fig. 2A**, B). Importantly, insulin-stimulated AKT phosphorylation in the liver was significantly improved in HFHS-fed $ATX^{+/-}$ mice compared with HFHS-fed WT mice, which was associated with reduced hepatic TG accumulation (supplemental Fig. S3E). Insulin-stimulated AKT phosphorylation was also unchanged in the PGAT of HFHS-fed $ATX^{+/-}$ mice compared with chow-fed $ATX^{+/-}$ mice (Fig. 2A, B), suggesting that $ATX^{+/-}$ mice are resistant to HFHS diet-induced insulin resistance in liver and PGAT. These results corresponded with insulin-stimulated p70S6K phosphorylation at T^{389} where p70S6K phosphorylation was higher in liver and PGAT from insulin-injected HFHS-fed $ATX^{+/-}$ mice compared with WT mice (supplemental Fig. S3A–C).

We next examined insulin signaling in cardiac and skeletal muscle. As with the liver, HFHS-fed WT mice showed markedly impaired insulin-stimulated AKT and p70S6K

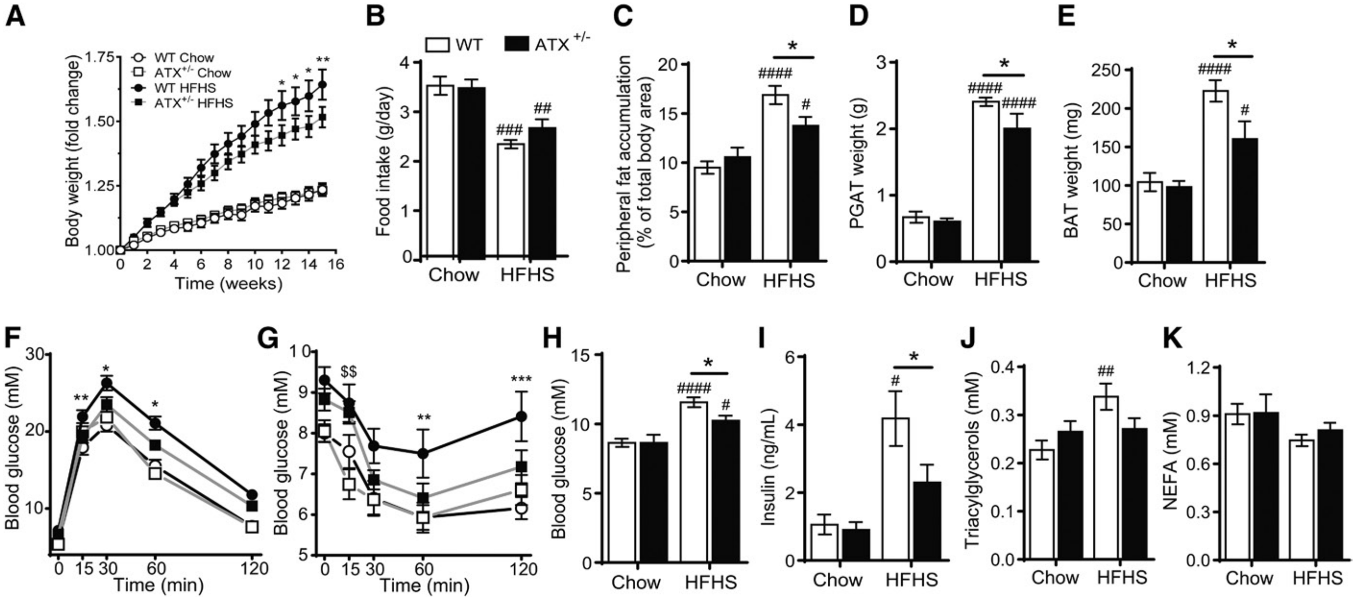

Fig. 1. Partial ATX deficiency protects from HFHS diet-induced obesity and metabolic dysfunction in male mice. Body weight gain (A), food intake (B), peripheral fat accumulation (C), PGAT weight (D), BAT weight (E), GTT following an intraperitoneal injection with D-glucose at 2 g/kg body weight (F), and ITT following an intraperitoneal injection with human insulin at 1 U/kg body weight (G) in chow- and HFHS-fed WT and $ATX^{+/-}$ mice (n = 14–26). Blood glucose (H) and serum insulin (I), TGs (J), and NEFA (K) in chow- and HFHS-fed WT and $ATX^{+/-}$ mice following a 3 h food withdrawal (n = 5–13). A–K: Statistical analysis was performed using a two-way ANOVA followed by a Tukey's multiple comparison test. A: $*P < 0.05$, $**P < 0.01$ versus $ATX^{+/-}$ HFHS. B–E, H–K: ${}^{\#}P < 0.05$, ${}^{\#\#}P < 0.01$, ${}^{\#\#\#}P < 0.001$, ${}^{\#\#\#\#}P < 0.0001$ versus chow; $*P < 0.05$ as indicated. F, G: $*P < 0.05$, $**P < 0.01$, $***P < 0.001$ for WT HFHS versus chow; ${}^{\$\$}P < 0.01$ for $ATX^{+/-}$ HFHS versus chow.

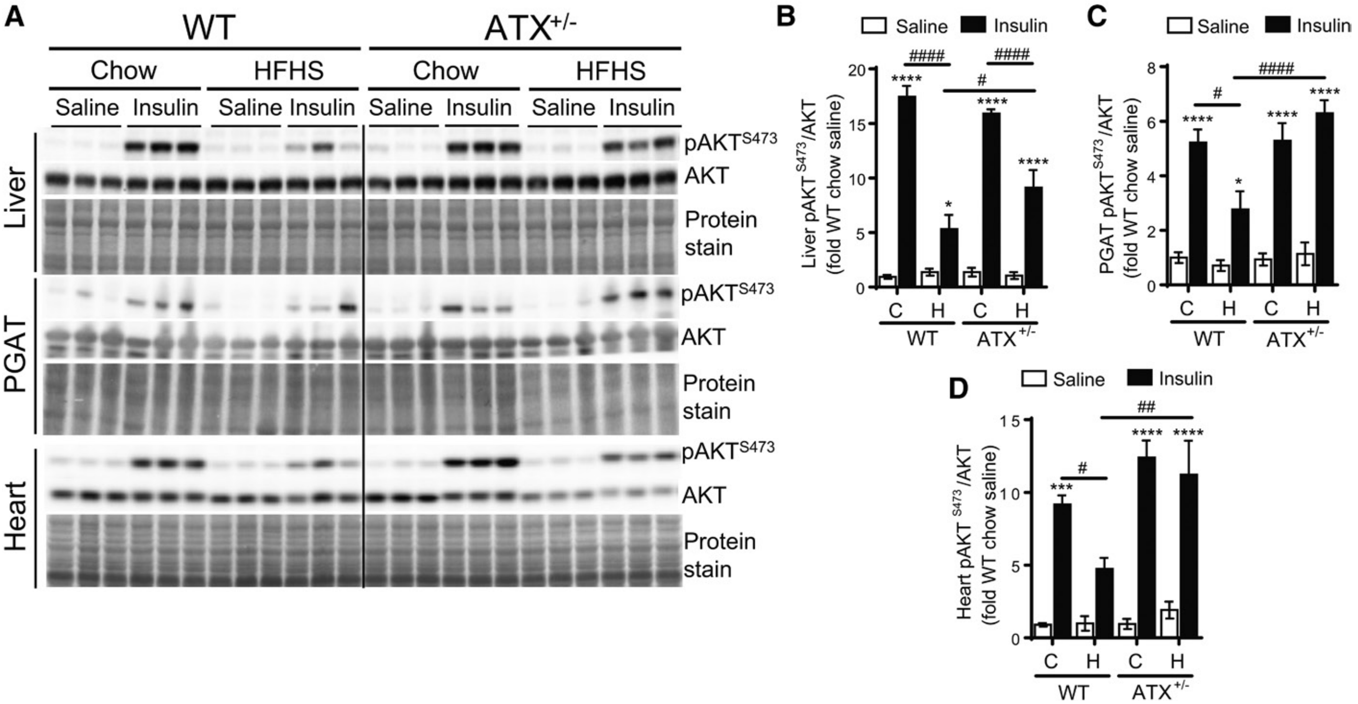

Fig. 2. HFHS-fed ATX$^{+/-}$ mice show improved insulin signaling in liver, PGAT, and heart. Immunoblot and densitometric analysis of AKT phosphorylation at S^{473} in liver (A, B), PGAT (A, C), and heart (A, D) from chow- and HFHS-fed male WT and ATX$^{+/-}$ mice subjected to a 3 h food withdrawal, followed by the intraperitoneal injection of saline or 10 U/kg insulin (n = 4–6). B–D: Statistical analysis was performed using a two-way ANOVA followed by a Tukey's multiple comparison test. *$P < 0.05$, ***$P < 0.001$, ****$P < 0.0001$ versus saline; $^{\#}P < 0.05$, $^{\#\#}P < 0.01$, $^{\#\#\#\#}P < 0.0001$ as indicated. C, chow; H, HFHS.

phosphorylation in the heart compared with chow-fed WT mice (Fig. 2A, D; supplemental Fig. S3A, D). AKT and p70S6K phosphorylation was unchanged in cardiac muscle from HFHS-fed ATX$^{+/-}$ mice compared with chow-fed controls (Fig. 2A, D; supplemental Fig. S3A, D). Preserved insulin-stimulated AKT phosphorylation in hearts from HFHS-fed ATX$^{+/-}$ mice was associated with a resistance toward HFHS diet-induced contractile dysfunction in cardiomyocytes isolated from ATX$^{+/-}$ mice (**Fig. 3A**–E). HFHS feeding led to a decrease in fractional shortening, rate of contraction, and rate of relaxation in cardiomyocytes from WT mice, but not ATX$^{+/-}$, mice (Fig. 3A–E).

Similar to cardiac muscle, insulin-stimulated AKT phosphorylation in the gastrocnemius and soleus muscle, which consist of primarily glycolytic and oxidative fibers, respectively, was improved in HFHS-fed ATX$^{+/-}$ mice compared with WT mice (**Fig. 4A**–C). In addition, gastrocnemius and soleus muscles from HFHS-fed ATX$^{+/-}$ mice were

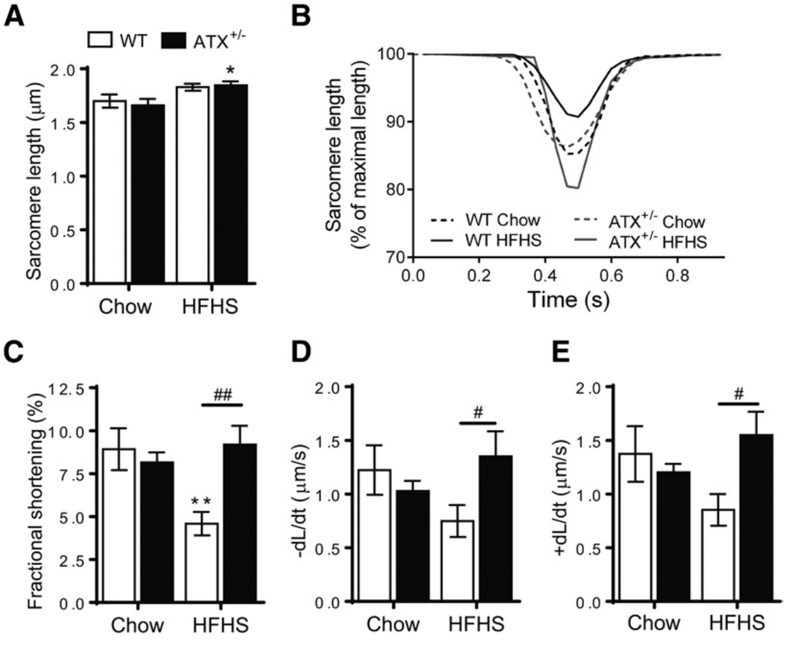

Fig. 3. Contractile properties are preserved in cardiomyocytes from HFHS-fed ATX$^{+/-}$ mice. Sarcomere length (A), sarcomere shortening trace (mean) (B), fractional shortening (C), sarcomere shortening rate (D), and sarcomere relengthening rate (E) in ventricular cardiomyocytes isolated from chow- and HFHS-fed male WT and ATX$^{+/-}$ mice (n = 7–12 cardiomyocytes from two to three mice per group, 10 contractions per cardiomyocyte). Statistical analysis was performed using a two-way ANOVA followed by a Sidak multiple comparison test. A, C–E: *$P < 0.05$, **$P < 0.01$ versus chow; $^{\#}P < 0.05$, $^{\#\#}P < 0.01$ as indicated.

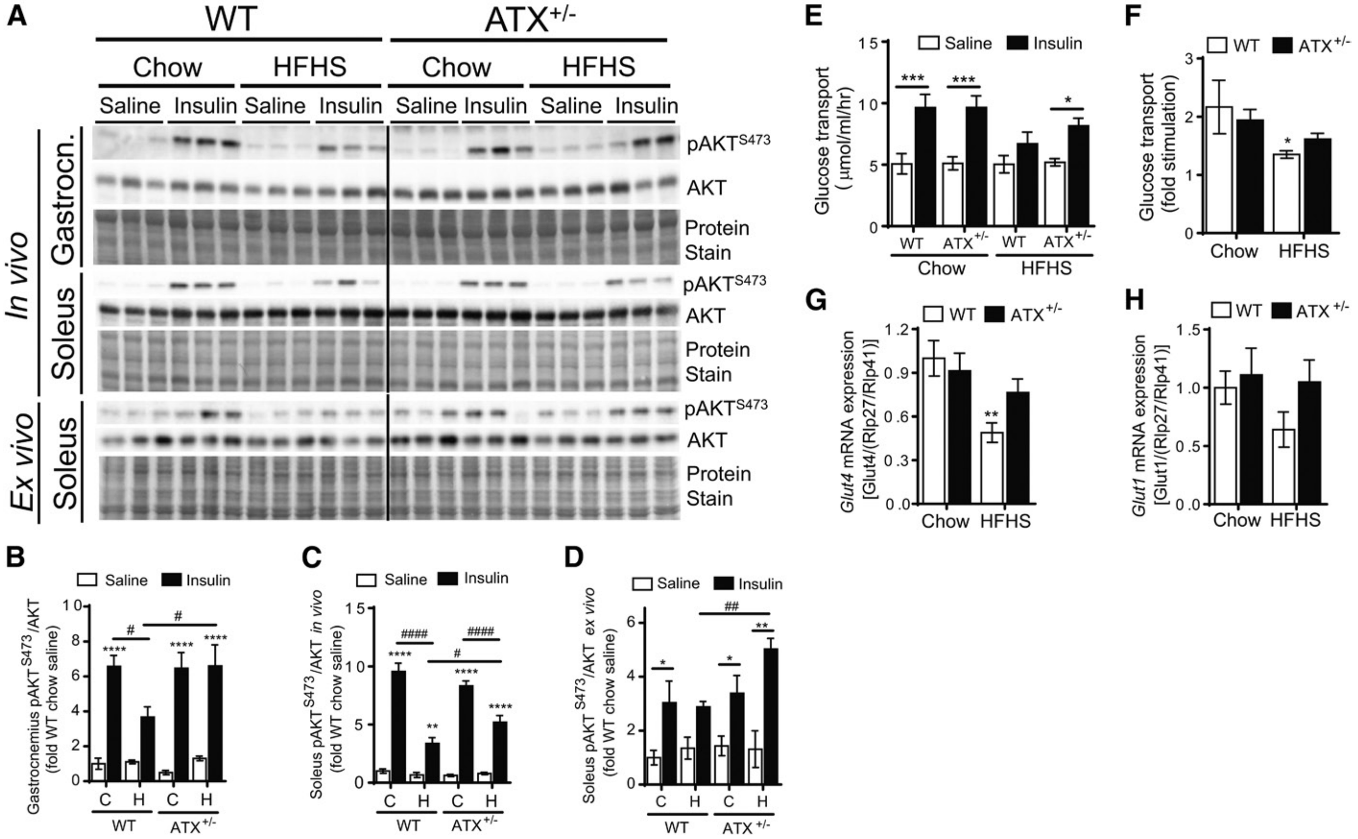

Fig. 4. HFHS-fed ATX$^{+/-}$ mice show improved insulin signaling in skeletal muscle in vivo and ex vivo. Immunoblot and densitometric analysis of AKT phosphorylation at S^{473} in gastrocnemius muscle (Gastrocn.) (A, B) and soleus muscle (A, C) from chow- and HFHS-fed male WT and ATX$^{+/-}$ mice subjected to a 3 h food withdrawal, followed by the intraperitoneal injection of saline or 10 U/kg insulin (n = 4–6). A, D: Immunoblot and densitometric analysis of AKT phosphorylation at S^{473} in soleus muscle isolated from chow- and HFHS-fed male WT and ATX$^{+/-}$ mice following incubation with saline or 33 nM insulin ex vivo (n = 3–5). Glucose transport rate (E) and fold stimulation (F) of glucose transport in soleus muscle from chow- and HFHS-fed male WT and ATX$^{+/-}$ mice incubated with saline or 33 nM insulin ex vivo. Gene expression analysis of *Glut4* (G) and *Glut1* (H) in soleus muscle from chow- and HFHS-fed male WT and ATX$^{+/-}$ mice (n = 7–10). B–H: Statistical analysis was performed using a two-way ANOVA followed by a Tukey's multiple comparison test. B–E: *$P < 0.05$, ***$P < 0.001$, ****$P < 0.0001$ versus saline; $^{\#}P < 0.05$, $^{\#\#\#\#}P < 0.0001$ as indicated. F–H: *$P < 0.05$, **$P < 0.01$ versus chow. C, chow; H, HFHS.

protected from impaired insulin-stimulated p70S6K phosphorylation (supplemental Fig. S3A, F, G). To determine whether improvements in skeletal muscle insulin signaling in HFHS-fed ATX$^{+/-}$ mice are maintained in the absence of circulating or neuronal factors, we performed insulin signaling analysis in soleus muscle ex vivo (Fig. 4A, D). Similar to improved insulin signaling in gastrocnemius and soleus muscles from HFHS-fed ATX$^{+/-}$ mice in vivo (Fig. 4A–C), insulin-stimulated AKT phosphorylation ex vivo was higher in soleus muscle from HFHS-fed ATX$^{+/-}$ mice than HFHS-fed WT mice (Fig. 4A, D). Furthermore, sustained muscle insulin signaling in HFHS-fed ATX$^{+/-}$ mice was associated with preserved insulin-stimulation of glucose transport in soleus muscle of HFHS-fed ATX$^{+/-}$ mice ex vivo, while the ability of insulin to stimulate glucose transport was reduced in soleus muscle from HFHS-fed WT mice compared with the chow control mice (Fig. 4E, F). In agreement with sustained insulin-stimulated glucose transport in HFHS-fed ATX$^{+/-}$ mice, soleus muscle from ATX$^{+/-}$ mice was protected from HFHS-induced decline of *Glut4* mRNA levels (Fig. 4G), while *Glut1* mRNA was unchanged between groups (Fig. 4H). Taken together, these data suggest that partial ATX deficiency protects against insulin resistance in metabolically active and insulin-responsive tissues, including liver, white adipose tissue, myocardium, and skeletal muscle. Our data also suggest that sustained insulin signaling in the heart underlies, in part, the resistance of cardiomyocytes from ATX$^{+/-}$ mice toward HFHS diet-induced contractile dysfunction. Moreover, our data suggest that preserved insulin stimulation of glucose transport in skeletal muscle contributes to the improved systemic glucose homeostasis in obese ATX$^{+/-}$ mice.

Improved insulin sensitivity in skeletal muscle of HFHS-fed ATX$^{+/-}$ mice is not associated with marked alterations in ectopic lipid accumulation

To explore possible mechanisms that underlie the blunted insulin resistance in skeletal muscle of HFHS-fed ATX$^{+/-}$ mice, we examined the accumulation of lipids that might contribute to obesity-induced muscle insulin resistance via lipidomic analysis in gastrocnemius muscle. Total ceramide levels were unchanged regardless of diet or genotype (**Fig. 5A**). When examining the major ceramide species, we noted a slight, but significant, decrease in unsaturated

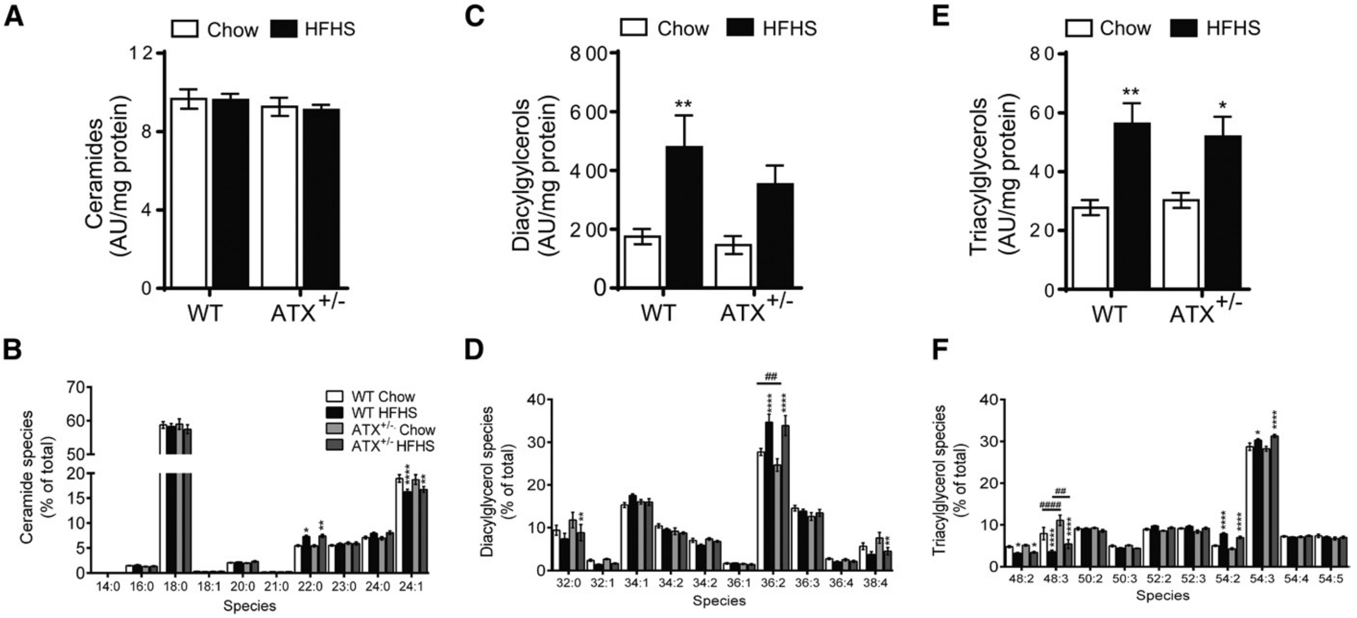

Fig. 5. HFHS-fed ATX$^{+/-}$ mice do not show marked changes in skeletal muscle lipid accumulation. Levels of total ceramides (A), ceramide species (B), total DGs (C), DG species (D), total TGs (E), and TG species (F) in gastrocnemius muscle from chow- and HFHS-fed male WT and ATX$^{+/-}$ mice subjected to a 3 h food withdrawal (n = 8). A–F: Statistical analysis was performed using a two-way ANOVA followed by a Tukey's multiple comparison test. $^{*}P < 0.05$, $^{**}P < 0.01$, $^{****}P < 0.0001$ versus chow; $^{\#\#}P < 0.01$, $^{\#\#\#\#}P < 0.0001$ as indicated.

species (24:1) and a shift toward saturated (22:0) species in HFHS-fed compared with chow-fed mice of both genotypes (Fig. 5B). Total DG levels increased 2.5-fold in HFHS-fed versus chow-fed WT mice (Fig. 5C). Total DG levels were similar between genotypes in both chow- and HFHS-fed states, although DG concentrations were not significantly increased in HFHS-fed versus chow-fed ATX$^{+/-}$ mice (Fig. 5C). When examining the DG acyl chain composition, we noted a HFHS diet-induced increase in 36:2 DGs in WT and ATX$^{+/-}$ mice, and a decrease in 32:0 and 38:4 DG species in HFHS-fed compared with chow-fed ATX$^{+/-}$ mice (Fig. 5D). Total TG levels were increased in HFHS-fed WT and ATX$^{+/-}$ mice compared with the chow-fed controls and were similar between genotypes (Fig. 5E). TG species analysis revealed a HFHS diet-induced increase in TGs with longer acyl chains (54:2 and 54:3) and a decrease in TGs with shorter acyl chains (48:2 and 48:3) (Fig. 5F). The 48:3 TGs were also changed between genotypes with lower levels detected in chow- and HFHS-fed ATX$^{+/-}$ mice compared with WT mice (Fig. 5F). Taken together, these data suggest that partial ATX deficiency modestly protects from obesity-induced increases in DG accumulation and results in altered TG species composition in skeletal muscle. These data also suggest that improved muscle insulin sensitivity in ATX$^{+/-}$ mice is not accompanied by major changes in muscle lipid accumulation.

Improved glucose homeostasis in HFHS-fed ATX$^{+/-}$ mice is associated with enhanced mitochondrial function in skeletal muscle

To determine whether improved mitochondrial function contributes to the improved glucose homeostasis and insulin sensitivity in muscle of HFHS-fed ATX$^{+/-}$ mice, we performed high-resolution respirometric analysis of mitochondria from permeabilized soleus muscle fibers (**Fig. 6A**, B, D, E). Interestingly, during pyruvate oxidation, mitochondria from HFHS-fed ATX$^{+/-}$ muscle showed a significant increase in respiratory oxygen consumption following the addition of ADP and succinate compared with chow-fed ATX$^{+/-}$ and HFHS-fed WT controls (Fig. 6A). These changes were not evident in HFHS-fed WT mice. Uncoupled respiration, induced by addition of carbonyl cyanide p-trifluoro-methoxyphenyl hydrazine (FCCP), was also significantly elevated in HFHS-fed ATX$^{+/-}$ muscle fibers (Fig. 6B). Increased mitochondrial respiration in the presence of pyruvate corresponded with increased citrate synthase activity in fibers from HFHS-fed ATX$^{+/-}$ mice (Fig. 6C), which is suggestive of elevated mitochondrial content (38). Mitochondrial respiration upon incubation with fatty acyl-carnitines was comparable between groups (Fig. 6D). Citrate synthase activity was reduced in fibers incubated with fatty acyl-carnitines and was not different between groups (data not shown), consistent with an inhibitory effect of fatty acyl esters on citrate synthase activity (39). Taken together, these data suggest that increased mitochondrial glucose/pyruvate oxidation is associated with blunted insulin resistance in skeletal muscle and contributes to improved glucose homeostasis in HFHS-fed ATX$^{+/-}$ mice.

LPA impairs insulin signaling and exacerbates palmitate-induced insulin resistance in C2C12 myotubes

We next sought to investigate whether the resistance of ATX$^{+/-}$ mice toward obesity-induced impairment of skeletal muscle insulin signaling is due to a direct effect of LPA on skeletal muscle insulin function. C2C12 myotubes were incubated for 18 h in the absence or presence of 1 and 10 μM 1-oleoyl-LPA, mimicking physiological and

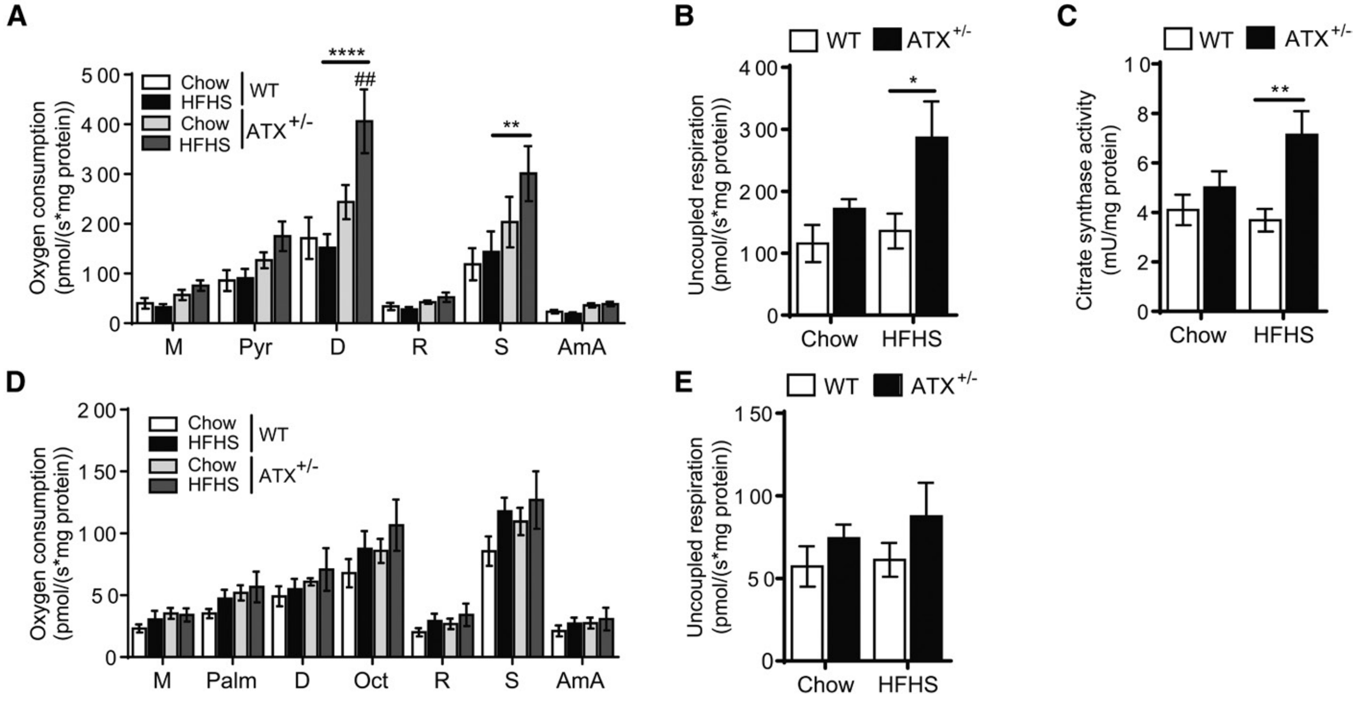

Fig. 6. Mitochondrial pyruvate oxidation is increased in skeletal muscle from HFHS-fed ATX$^{+/-}$ mice. Mitochondrial respiration (A, D) and uncoupled respiration (B, E) during pyruvate oxidation (A, B) and fatty acid oxidation (D, E) in permeabilized soleus muscle fibers from chow- and HFHS-fed male WT and ATX$^{+/-}$ mice. C: Citrate synthase activity in fibers subjected to pyruvate oxidation analysis (n = 5–6). A–E: Statistical analysis was performed using a two-way ANOVA followed by a Tukey's multiple comparison test. $^{\#\#}P < 0.01$ versus chow; $*P < 0{,}05$, $**P < 0.01$, $****P < 0.0001$ as indicated. M, malate; Pyr, pyruvate; Palm, palmitoyl-carnitine; D, ADP; Oct, octanoyl-carnitine; R, rotenone; S, succinate; AmA, antimycin A.

pathophysiological LPA concentrations (1, 4, 5, 40) (supplemental Fig. S1A). Cells were also simultaneously incubated in the absence or presence of 0.8 mM palmitate to induce insulin resistance, as determined by a 2-fold reduction in insulin-stimulated AKT phosphorylation at S^{473} (**Fig. 7A**, B). At baseline, incubation with LPA impaired insulin-stimulated AKT phosphorylation in C2C12 myotubes, similar to palmitate (Fig. 7A, B). Moreover, LPA exacerbated the palmitate-induced reduction in insulin-stimulated AKT phosphorylation (Fig. 7A, B). Prolonged treatment of C2C12 cells with LPA has been linked to the activation of JNK and ERK, both of which are associated with the development of insulin resistance (41–43). Consistent with this notion, LPA-induced impairment of insulin function and exacerbation of palmitate-induced insulin resistance in C2C12 cells was associated with an upregulation of JNK and ERK phosphorylation (Fig. 7A, C, D). Taken together, these data suggest that exposure of muscle cells to LPA directly promotes the development of insulin resistance and worsens impaired insulin signaling induced by a lipotoxic milieu.

LPA impairs mitochondrial respiration in C2C12 myotubes

To determine whether exogeneous LPA modulates mitochondrial function in muscle cells, insulin-sensitive and insulin-resistant C2C12 myotubes were incubated with LPA and subjected to respirometric analysis (**Fig. 8A**, B). Insulin-resistant C2C12 myotubes showed significantly reduced mitochondrial respiration in the presence of fatty acyl carnitines and pyruvate compared with insulin-sensitive cells (Fig. 8A). Addition of LPA in insulin-resistant myotubes further depressed mitochondrial respiration (Fig. 8A). LPA also had an effect on mitochondrial respiration in insulin-sensitive myotubes, leading to a significant reduction in pyruvate-supported mitochondrial O_2 flow (Fig. 8A). Moreover, LPA treatment significantly reduced uncoupled respiration in insulin-resistant myotubes (Fig. 8B). In accordance with increased citrate synthase activity in muscle from HFHS-fed ATX$^{+/-}$ mice (Fig. 6C), incubation with LPA reduced citrate synthase activity in insulin-sensitive and insulin-resistant myotubes, consistent with impaired mitochondrial respiration (Fig. 8C). Taken together, these data suggest that LPA directly impairs mitochondrial function in C2C12 myotubes.

DISCUSSION

Recent studies have implicated the ATX-LPA axis in obesity and impaired glucose homeostasis (4, 5, 19–21, 23). Improvements in obesity-induced insulin resistance and glucose intolerance in ATX mutant mice were primarily ascribed to changes in adipose tissue metabolism and function (4, 5). It remained unclear whether changes in insulin signaling and mitochondrial function in metabolically relevant tissues contribute to the protective effect of ATX deficiency toward the obesity-induced impairment of glucose homeostasis. In this study, we show that amelioration of obesity and systemic insulin resistance in HFHS-fed mice

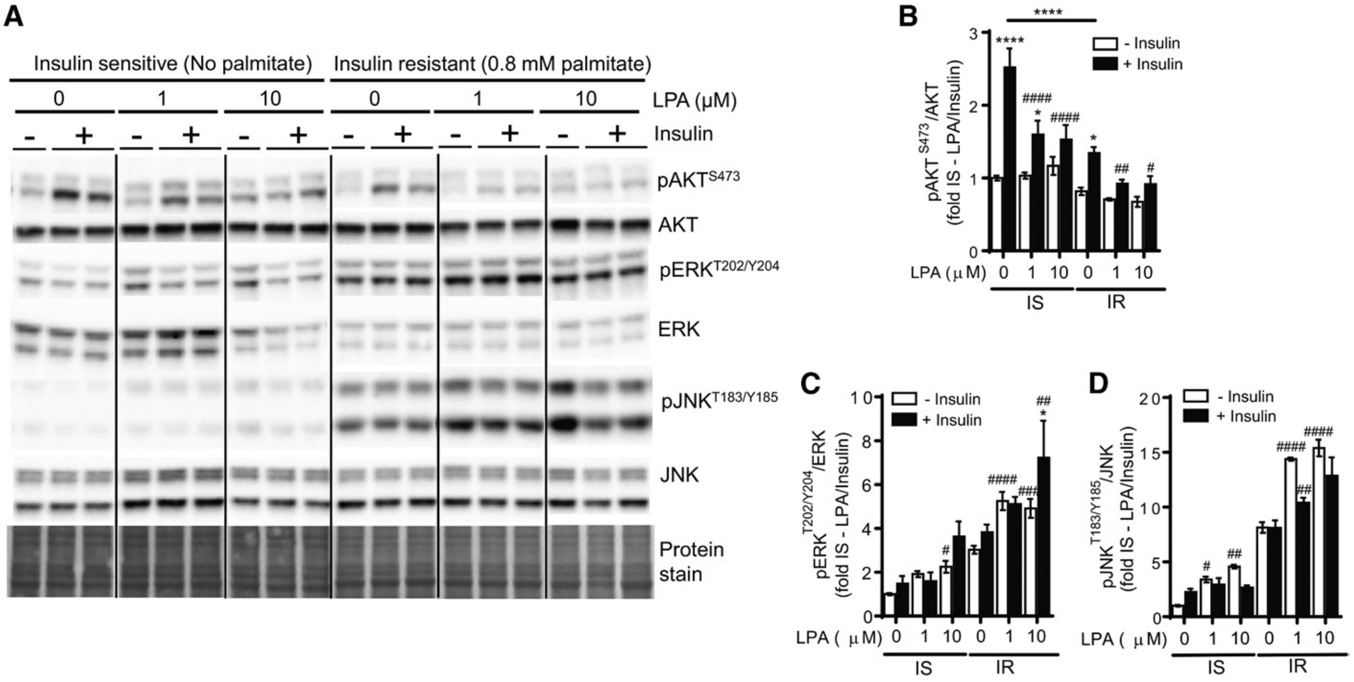

Fig. 7. LPA impairs insulin signaling and exacerbates palmitate-induced insulin resistance in C2C12 myotubes. Immunoblot and densitometric analysis of AKT phosphorylation at S^{473} (A, B), ERK phosphorylation at T^{202}/Y^{204} (A, C), and JNK phosphorylation at T^{T183}/Y^{185} (A, D) in C2C12 myotubes incubated in the absence or presence of 0.8 mM palmitate and 0, 1, or 10 μM LPA for 18 h, followed by stimulation with 20 nM insulin for 15 min (n = 6). B–D: Statistical analysis was performed using a two-way ANOVA followed by a Tukey's multiple comparison test. *$P < 0.05$, ****$P < 0.0001$ versus saline; $^{\#}P < 0.05$, $^{\#\#}P < 0.01$, $^{\#\#\#}P < 0.001$, $^{\#\#\#\#}P < 0.0001$ versus no LPA controls. IS, insulin sensitive; IR, insulin resistant.

with partial ATX deficiency is associated with increased insulin signaling in metabolically active tissues, including liver, adipose tissue, and heart, as well as protection from obesity-induced cardiomyocyte dysfunction. In skeletal muscle, which accounts for the majority of insulin-stimulated glucose disposal (25), partial ATX deficiency led to improvements in insulin signaling and insulin-stimulated glucose transport following HFHS feeding. In C2C12 myotubes, LPA directly impaired insulin signaling and exacerbated palmitate-induced insulin resistance. Our data also show that the ATX-LPA axis influences mitochondrial metabolism in muscle because partial ATX deficiency resulted in enhanced mitochondrial pyruvate/glucose oxidation in HFHS-fed mice and LPA directly decreased mitochondrial pyruvate/glucose oxidation in C2C12 myotubes. Impaired mitochondrial metabolism was paralleled by corresponding changes in citrate synthase activity, an indicator of mitochondrial function and abundance. Taken together, these data suggest that the ATX-LPA pathway plays an important role in the development of obesity-induced insulin resistance and impairs mitochondrial metabolism in skeletal muscle.

Only a few prior studies have examined the effect of ATX-LPA signaling on tissue insulin function (21, 24, 44). Rancoule et al. (24) showed that administration of a LPA1/3 receptor antagonist in high-fat diet-fed mice for 3 weeks improves insulin sensitivity and increases insulin-stimulated glucose oxidation in muscle ex vivo, suggesting

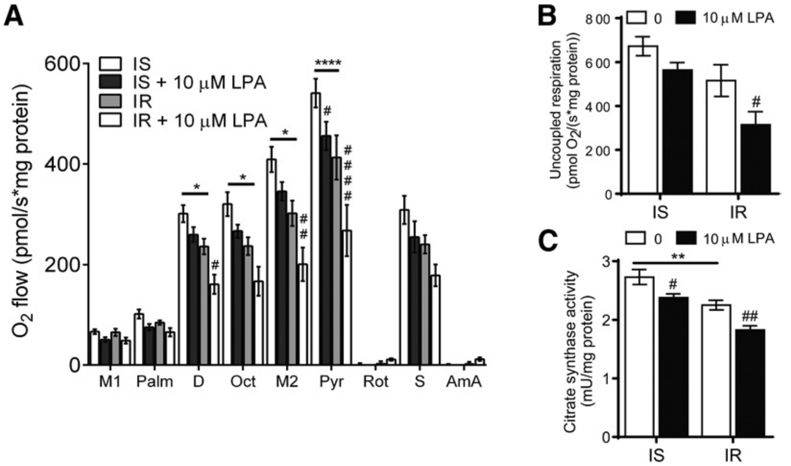

Fig. 8. LPA impairs mitochondrial respiration in C2C12 myotubes. Mitochondrial respiration (A), uncoupled respiration (B), and citrate synthase activity (C) in permeabilized C2C12 myotubes incubated in the absence or presence of 0.8 mM palmitate and 0 or 10 μM LPA for 18 h (n = 5–6). A–C: Statistical analysis was performed using a two-way ANOVA followed by a Tukey's multiple comparison test. *$P < 0.05$, **$P < 0.01$, ****$P < 0.0001$ versus insulin sensitive; $^{\#}P < 0.05$, $^{\#\#}P < 0.01$, $^{\#\#\#\#}P < 0.0001$ versus no LPA controls. IS, insulin sensitive; IR, insulin resistant. M1/2, malate; Palm, palmitoyl-carnitine; D, ADP; Oct, octanoyl-carnitine; Pyr, pyruvate; R, rotenone; S, succinate; AmA, antimycin A.

that LPA signaling through LPA1/3 impairs muscle insulin function. However, other effects of systemic LPA1/3 inhibition, including increased pancreatic islet mass and liver glycogen storage, may have contributed to changes in glucose metabolism in muscle (24). Two very recent studies have provided more direct evidence for an inhibitory role of ATX-LPA signaling on tissue insulin function (21, 44). Acute pretreatment of primary rat hepatocytes with LPA decreased insulin-stimulated AKT phosphorylation, glucokinase, and SREBP-1c expression, PI3K activation, and glycogen synthesis, likely via LPA1 and/or LPA3 (44). Moreover, inhibition of ATX protected against interleukin 6-induced impairment of insulin-stimulated AKT phosphorylation in 3T3-L1 adipocytes (21). We have previously shown that 24 h inhibition of ATX in 3T3-L1 adipocytes exposed to high glucose and insulin does not alter insulin resistance (22). However, it is possible that prolonged ATX inhibition is necessary to alter insulin signaling in this insulin-resistant adipocyte model. In this study, we show that reduced ATX function ameliorates insulin resistance in adipose tissue, liver, heart, and skeletal muscle in vivo. Incubation with LPA directly impairs insulin signaling in myotubes, possibly through activation of JNK, ERK, or other stress kinases (41). Future studies should identify the LPA receptor(s) and precise mechanisms that mediate LPA-induced muscle insulin resistance. It is possible that Gα13, a mediator downstream of most LPA receptors (13), plays a role in the inhibition of muscle insulin function by LPA because Gα13 impairs muscle glucose uptake and systemic insulin sensitivity in high-fat diet-fed mice (45).

Insulin resistance has been linked to altered mitochondrial function, although it remains uncertain whether changes in mitochondrial capacity are a cause or a consequence of insulin resistance (46). The ATX-LPA axis appears to impair mitochondrial function in BAT (5, 23). Microarray analysis of primary BAT preadipocytes differentiated with LPA or ATX inhibitor revealed that the ATX-LPA pathway decreases the expression of many genes involved in mitochondrial function (23). Consistent with this observation, a study employing mice with adipose-specific ATX deficiency also suggested that the ATX-LPA pathway decreases mitochondrial content and membrane potential in BAT at baseline and following diet-induced obesity (5). However, it is presently unclear whether the ATX-LPA-induced decrease in mitochondrial function in BAT is secondary to changes in preadipocyte differentiation (5, 23). Our study suggests that the ATX-LPA pathway plays a role in modulating mitochondrial function during insulin resistance by reducing oxidative metabolism and decreasing citrate synthase activity, an indicator of mitochondrial density, in muscle. Our data also suggest that partial ATX deficiency in vivo selectively increases mitochondrial pyruvate oxidation following diet-induced obesity. Unaltered fat oxidation in muscle from HFHS-fed ATX$^{+/-}$ mice may explain the absence of major changes in muscle lipid accumulation, despite an overall decrease in obesity in these mice. Because we assessed muscle lipid accumulation in mice subjected to a 3 h food withdrawal, it remains to be determined whether lipid levels are also similar between genotypes following prolonged fasting. Nevertheless, these data confirm a study by Nishimura et al. (5) showing that ectopic fat accumulation in skeletal muscle, liver, and heart was similar in WT and ATX$^{+/-}$ mice with diet-induced obesity. Besides affecting insulin signaling, the ATX-LPA pathway has also been suggested to modulate other important processes in skeletal muscle, including the migration of satellite cells (47), secretion of chemokines (48), and regulation of intracellular calcium levels (49). It would be interesting to determine whether ameliorated insulin resistance in skeletal muscle from ATX$^{+/-}$ mice is linked to changes in these processes in vivo.

Taken together, our study suggests that, in addition to reduced adipose tissue accumulation, improved insulin signaling in adipose tissue, liver, and muscle contributes to preserved global insulin sensitivity in mice with partial ATX deficiency. Our data also suggest that the ATX-LPA pathway directly impairs insulin signaling, insulin-stimulated glucose transport, and mitochondrial function in skeletal muscle (**Fig. 9**). Because impaired insulin signaling and metabolism in skeletal muscle are primary drivers of systemic insulin resistance and hyperglycemia (50), we propose that the obesity-induced upregulation of ATX and LPA receptor signaling in muscle are critical mechanisms of insulin resistance. Therefore, modulators of the ATX-LPA pathway

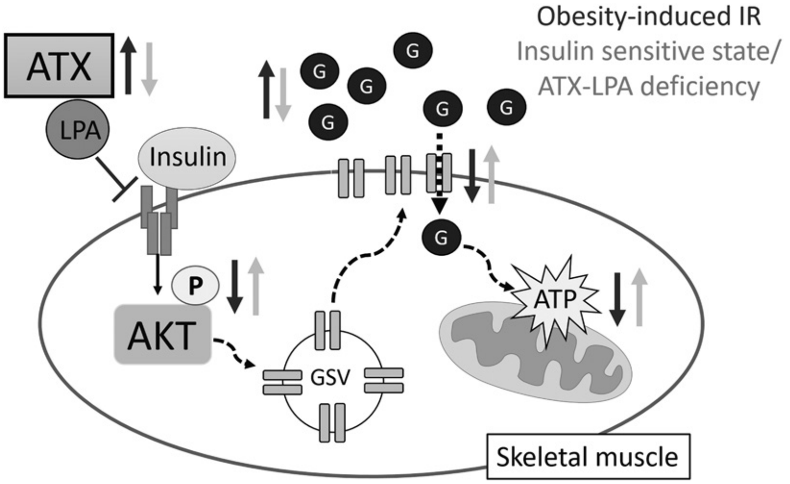

Fig. 9. Proposed role of the ATX-LPA axis in skeletal muscle insulin signaling and mitochondrial function. In diet-induced obesity, increases in ATX-LPA contribute to impaired skeletal muscle insulin signaling and glucose transport, a primary driver of systemic insulin resistance and type 2 diabetes. Inhibition of the ATX-LPA pathway enhances skeletal muscle insulin signaling, glucose transport, and mitochondrial glucose oxidation in an obesogenic milieu, thereby ameliorating diet-induced obesity and glucose homeostasis. GSV, Glut4 storage vesicles; P, phosphorylation; G, glucose.

may present novel strategies toward the prevention and treatment of obesity-associated insulin resistance and type 2 diabetes.

The authors thank Angella Mercer for technical assistance.

REFERENCES

1. Benesch, M. G., Y. M. Ko, T. P. McMullen, and D. N. Brindley. 2014. Autotaxin in the crosshairs: taking aim at cancer and other inflammatory conditions. *FEBS Lett.* **588:** 2712–2727.
2. Okudaira, S., H. Yukiura, and J. Aoki. 2010. Biological roles of lysophosphatidic acid signaling through its production by autotaxin. *Biochimie.* **92:** 698–706.
3. Aoki, J., A. Taira, Y. Takanezawa, Y. Kishi, K. Hama, T. Kishimoto, K. Mizuno, K. Saku, R. Taguchi, and H. Arai. 2002. Serum lysophosphatidic acid is produced through diverse phospholipase pathways. *J. Biol. Chem.* **277:** 48737–48744.
4. Dusaulcy, R., C. Rancoule, S. Gres, E. Wanecq, A. Colom, C. Guigne, L. A. van Meeteren, W. H. Moolenaar, P. Valet, and J. S. Saulnier-Blache. 2011. Adipose-specific disruption of autotaxin enhances nutritional fattening and reduces plasma lysophosphatidic acid. *J. Lipid Res.* **52:** 1247–1255.
5. Nishimura, S., M. Nagasaki, S. Okudaira, J. Aoki, T. Ohmori, R. Ohkawa, K. Nakamura, K. Igarashi, H. Yamashita, K. Eto, et al. 2014. ENPP2 contributes to adipose tissue expansion in diet-induced obesity. *Diabetes.* **63:** 4154–4164.
6. Yung, Y. C., N. C. Stoddard, and J. Chun. 2014. LPA receptor signaling: pharmacology, physiology, and pathophysiology. *J. Lipid Res.* **55:** 1192–1214.
7. Lin, M. E., D. R. Herr, and J. Chun. 2010. Lysophosphatidic acid (LPA) receptors: signaling properties and disease relevance. *Prostaglandins Other Lipid Mediat.* **91:** 130–138.
8. Abdel-Latif, A., P. M. Heron, A. J. Morris, and S. S. Smyth. 2015. Lysophospholipids in coronary artery and chronic ischemic heart disease. *Curr. Opin. Lipidol.* **26:** 432–437.
9. Chun, J., T. Hla, K. R. Lynch, S. Spiegel, and W. H. Moolenaar. 2010. International Union of Basic and Clinical Pharmacology. LXXVIII. Lysophospholipid receptor nomenclature. *Pharmacol. Rev.* **62:** 579–587.
10. Kaffe, E., A. Katsifa, N. Xylourgidis, I. Ninou, M. Zannikou, V. Harokopos, P. Foka, A. Dimitriadis, K. Evangelou, A. N. Moulas, et al. 2017. Hepatocyte autotaxin expression promotes liver fibrosis and cancer. *Hepatology.* **65:** 1369–1383.
11. Oikonomou, N., M. A. Mouratis, A. Tzouvelekis, E. Kaffe, C. Valavanis, G. Vilaras, A. Karameris, G. D. Prestwich, D. Bouros, and V. Aidinis. 2012. Pulmonary autotaxin expression contributes to the pathogenesis of pulmonary fibrosis. *Am. J. Respir. Cell Mol. Biol.* **47:** 566–574.
12. Nikitopoulou, I., N. Oikonomou, E. Karouzakis, I. Sevastou, N. Nikolaidou-Katsaridou, Z. Zhao, V. Mersinias, M. Armaka, Y. Xu, M. Masu, et al. 2012. Autotaxin expression from synovial fibroblasts is essential for the pathogenesis of modeled arthritis. *J. Exp. Med.* **209:** 925–933.
13. Stoddard, N. C., and J. Chun. 2015. Promising pharmacological directions in the world of lysophosphatidic Acid signaling. *Biomol. Ther. (Seoul).* **23:** 1–11.
14. Barbayianni, E., E. Kaffe, V. Aidinis, and G. Kokotos. 2015. Autotaxin, a secreted lysophospholipase D, as a promising therapeutic target in chronic inflammation and cancer. *Prog. Lipid Res.* **58:** 76–96.
15. Kihara, Y., H. Mizuno, and J. Chun. 2015. Lysophospholipid receptors in drug discovery. *Exp. Cell Res.* **333:** 171–177.
16. Katsifa, A., E. Kaffe, N. Nikolaidou-Katsaridou, A. N. Economides, S. Newbigging, C. McKerlie, and V. Aidinis. 2015. The bulk of autotaxin activity is dispensable for adult mouse life. *PLoS One.* **10:** e0143083.
17. Ferry, G., E. Tellier, A. Try, S. Gres, I. Naime, M. F. Simon, M. Rodriguez, J. Boucher, I. Tack, S. Gesta, et al. 2003. Autotaxin is released from adipocytes, catalyzes lysophosphatidic acid synthesis, and activates preadipocyte proliferation. Up-regulated expression with adipocyte differentiation and obesity. *J. Biol. Chem.* **278:** 18162–18169.
18. Boucher, J., D. Quilliot, J. P. Praderes, M. F. Simon, S. Gres, C. Guigne, D. Prevot, G. Ferry, J. A. Boutin, C. Carpene, et al. 2005. Potential involvement of adipocyte insulin resistance in obesity-associated up-regulation of adipocyte lysophospholipase D/autotaxin expression. *Diabetologia.* **48:** 569–577.
19. Rachakonda, V. P., V. L. Reeves, J. Aljammal, R. C. Wills, J. S. Trybula, J. P. DeLany, P. C. Kienesberger, and E. E. Kershaw. 2015. Serum autotaxin is independently associated with hepatic steatosis in women with severe obesity. *Obesity (Silver Spring).* **23:** 965–972.
20. Reeves, V. L., J. S. Trybula, R. C. Wills, B. H. Goodpaster, J. J. Dube, P. C. Kienesberger, and E. E. Kershaw. 2015. Serum autotaxin/ENPP2 correlates with insulin resistance in older humans with obesity. *Obesity (Silver Spring).* **23:** 2371–2376.
21. Sun, S., R. Wang, J. Song, M. Guan, N. Li, X. Zhang, Z. Zhao, and J. Zhang. 2017. Blocking gp130 signaling suppresses autotaxin expression in adipocytes and improves insulin sensitivity in diet-induced obesity. *J. Lipid Res.* **58:** 2102–2113.
22. D'Souza, K., D. A. Kane, M. Touaibia, E. E. Kershaw, T. Pulinilkunnil, and P. C. Kienesberger. 2017. Autotaxin is regulated by glucose and insulin in adipocytes. *Endocrinology.* **158:** 791–803.
23. Federico, L., H. Ren, P. A. Mueller, T. Wu, S. Liu, J. Popovic, E. M. Blalock, M. Sunkara, H. Ovaa, H. M. Albers, et al. 2012. Autotaxin and its product lysophosphatidic acid suppress brown adipose differentiation and promote diet-induced obesity in mice. *Mol. Endocrinol.* **26:** 786–797.
24. Rancoule, C., C. Attane, S. Gres, A. Fournel, R. Dusaulcy, C. Bertrand, C. Vinel, K. Treguer, M. Prentki, P. Valet, et al. 2013. Lysophosphatidic acid impairs glucose homeostasis and inhibits insulin secretion in high-fat diet obese mice. *Diabetologia.* **56:** 1394–1402.
25. Abdul-Ghani, M. A., and R. A. DeFronzo. 2010. Pathogenesis of insulin resistance in skeletal muscle. *J. Biomed. Biotechnol.* **2010:** 476279.
26. Fotopoulou, S., N. Oikonomou, E. Grigorieva, I. Nikitopoulou, T. Paparountas, A. Thanassopoulou, Z. Zhao, Y. Xu, D. L. Kontoyiannis, E. Remboutsika, et al. 2010. ATX expression and LPA signalling are vital for the development of the nervous system. *Dev. Biol.* **339:** 451–464.
27. Kienesberger, P. C., D. Lee, T. Pulinilkunnil, D. S. Brenner, L. Cai, C. Magnes, H. C. Koefeler, I. E. Streith, G. N. Rechberger, G. Haemmerle, et al. 2009. Adipose triglyceride lipase deficiency causes tissue-specific changes in insulin signaling. *J. Biol. Chem.* **284:** 30218–30229.
28. Perez, L. J., L. Rios, P. Trivedi, K. D'Souza, A. Cowie, C. Nzirorera, D. Webster, K. Brunt, J. F. Legare, A. Hassan, et al. 2017. Validation of optimal reference genes for quantitative real time PCR in muscle and adipose tissue for obesity and diabetes research. *Sci. Rep.* **7:** 3612.
29. Kraemer, M. P., S. Halder, S. S. Smyth, and A. J. Morris. 2018. Measurement of lysophosphatidic acid and sphingosine-1-phosphate by liquid chromatography-coupled electrospray ionization tandem mass spectrometry. *Methods Mol. Biol.* **1697:** 31–42.
30. Benesch, M. G., Y. Y. Zhao, J. M. Curtis, T. P. McMullen, and D. N. Brindley. 2015. Regulation of autotaxin expression and secretion by lysophosphatidate and sphingosine 1-phosphate. *J. Lipid Res.* **56:** 1134–1144.
31. St-Cœur, P. D., D. Ferguson, P. Morin, Jr., and M. Touaibia. 2013. PF-8380 and closely related analogs: synthesis and structure-activity relationship towards autotaxin inhibition and glioma cell viability. *Arch. Pharm. (Weinheim).* **346:** 91–97.
32. Kuznetsov, A. V., V. Veksler, F. N. Gellerich, V. Saks, R. Margreiter, and W. S. Kunz. 2008. Analysis of mitochondrial function in situ in permeabilized muscle fibers, tissues and cells. *Nat. Protoc.* **3:** 965–976.
33. Boudina, S., S. Sena, B. T. O'Neill, P. Tathireddy, M. E. Young, and E. D. Abel. 2005. Reduced mitochondrial oxidative capacity and increased mitochondrial uncoupling impair myocardial energetics in obesity. *Circulation.* **112:** 2686–2695.
34. Folch, J., M. Lees, and G. H. Sloane Stanley. 1957. A simple method for the isolation and purification of total lipides from animal tissues. *J. Biol. Chem.* **226:** 497–509.
35. Knittelfelder, O. L., B. P. Weberhofer, T. O. Eichmann, S. D. Kohlwein, and G. N. Rechberger. 2014. A versatile ultra-high performance LC-MS method for lipid profiling. *J. Chromatogr. B Analyt. Technol. Biomed. Life Sci.* **951–952:** 119–128.
36. Pulinilkunnil, T., P. C. Kienesberger, J. Nagendran, N. Sharma, M. E. Young, and J. R. Dyck. 2014. Cardiac-specific adipose triglyceride

lipase overexpression protects from cardiac steatosis and dilated cardiomyopathy following diet-induced obesity. *Int. J. Obes. (Lond.).* **38:** 205–215.

37. Bartlett, J. J., P. C. Trivedi, P. Yeung, P. C. Kienesberger, and T. Pulinilkunnil. 2016. Doxorubicin impairs cardiomyocyte viability by suppressing transcription factor EB expression and disrupting autophagy. *Biochem. J.* **473:** 3769–3789.
38. Larsen, S., J. Nielsen, C. N. Hansen, L. B. Nielsen, F. Wibrand, N. Stride, H. D. Schroder, R. Boushel, J. W. Helge, F. Dela, et al. 2012. Biomarkers of mitochondrial content in skeletal muscle of healthy young human subjects. *J. Physiol.* **590:** 3349–3360.
39. Else, A. J., S. J. Barnes, M. J. Danson, and P. D. Weitzman. 1988. A new spectrophotometric assay for citrate synthase and its use to assess the inhibitory effects of palmitoyl thioesters. *Biochem. J.* **251:** 803–807.
40. D'Souza K., G. V. Paramel, and P. C. Kienesberger. 2018. Lysophosphatidic acid signaling in obesity and insulin resistance. *Nutrients.* **10:** E399.
41. Jean-Baptiste, G., Z. Yang, C. Khoury, and M. T. Greenwood. 2005. Lysophosphatidic acid mediates pleiotropic responses in skeletal muscle cells. *Biochem. Biophys. Res. Commun.* **335:** 1155–1162.
42. Masharani, U. B., B. A. Maddux, X. Li, G. K. Sakkas, K. Mulligan, M. Schambelan, I. D. Goldfine, and J. F. Youngren. 2011. Insulin resistance in non-obese subjects is associated with activation of the JNK pathway and impaired insulin signaling in skeletal muscle. *PLoS One.* **6:** e19878.
43. Fujishiro, M., Y. Gotoh, H. Katagiri, H. Sakoda, T. Ogihara, M. Anai, Y. Onishi, H. Ono, M. Abe, N. Shojima, et al. 2003. Three mitogen-activated protein kinases inhibit insulin signaling by different mechanisms in 3T3–L1 adipocytes. *Mol. Endocrinol.* **17:** 487–497.
44. Fayyaz, S., L. Japtok, F. Schumacher, D. Wigger, T. J. Schulz, K. Haubold, E. Gulbins, H. Voller, and B. Kleuser. 2017. Lysophosphatidic acid inhibits insulin signaling in primary rat hepatocytes via the LPA3 receptor subtype and is increased in obesity. *Cell. Physiol. Biochem.* **43:** 445–456.
45. Koo, J. H., T. H. Kim, S. Y. Park, M. S. Joo, C. Y. Han, C. S. Choi, and S. G. Kim. 2017. Galpha13 ablation reprograms myofibers to oxidative phenotype and enhances whole-body metabolism. *J. Clin. Invest.* **127:** 3845–3860.
46. Montgomery, M. K., and N. Turner. 2015. Mitochondrial dysfunction and insulin resistance: an update. *Endocr. Connect.* **4:** R1–R15.
47. Cencetti, F., G. Bruno, S. Blescia, C. Bernacchioni, P. Bruni, and C. Donati. 2014. Lysophosphatidic acid stimulates cell migration of satellite cells. A role for the sphingosine kinase/sphingosine 1-phosphate axis. *FEBS J.* **281:** 4467–4478.
48. Tsukahara, T., and H. Haniu. 2012. Lysophosphatidic acid stimulates MCP-1 secretion from C2C12 Myoblast. *ISRN Inflamm.* **2012:** 983420.
49. Xu, Y. J., P. S. Tappia, R. K. Goyal, and N. S. Dhalla. 2008. Mechanisms of the lysophosphatidic acid-induced increase in [Ca(2+)](i) in skeletal muscle cells. *J. Cell. Mol. Med.* **12:** 942–954.
50. DeFronzo, R. A., and D. Tripathy. 2009. Skeletal muscle insulin resistance is the primary defect in type 2 diabetes. *Diabetes Care.* **32(Suppl 2):** S157–S163.